Research Article

Design of TiO_2-based nanocomposite via two-step method on Al- and Fe-doped Ti_3SiC_2 ceramic for photoelectrode

Zhiwei Wang[1] · Hongfeng Yin[1] · Yun Tang[1] · Xiaohu Ren[1] · Hudie Yuan[1] · Nan Yan[1]

Received: 11 December 2019 / Accepted: 7 May 2020 / Published online: 25 May 2020

Abstract
Photocapacitors gain increasing attention due to their capability of integrating conversion and storage of solar energy which can realize miniaturization and multi-functionalization of the device. In this work, a photoresponsible and reliable electrode consisting of Al- and Fe-doped TiO_2 (Al, Fe–TiO_2), SiO_2 and C with vertically aligned nanopores structure is developed on a pentabasic ceramic substrate of Al- and Fe-doped Ti_3SiC_2 (Al, Fe–TSC) via sintering and anodizing in sequence. The resulting electrode demonstrates good electrochemical performance with a specific capacitance of 12.03 mF cm^{-2} at the scan rate of 100 mV s^{-1} and sustains a stability of 93% after 1000 cycles. Moreover, it exhibits a high solar energy conversion and storage capacity up to 59 μA cm^{-2} and 4.33 mF cm^{-2} under visible light irradiation indicating that it has the potential to be used as a photocapacitor. The exploited approach in this work offers an alternative strategy for designing miniaturized difunctional photoelectrode ingredients with ordered periodic nanostructure to promote solar harvesting and utilizing of the photocapacitor.

Keywords TiO_2 · Photoelectrode · Anodization · Doping · Capacitor

1 Introduction

The clean and sustainable solar energy is a sensible alternative to the dwindling stocks of nonrenewable fuels which emit environmentally detrimental gases [1, 2]. For efficient utilization of solar energy, recent emergence of an integrated device named as photocapacitor has received tremendous attention due to their ability to generate, transport and store charges simultaneously, which is first devised by Miyasaka [3]. Over the past few years of research, dye-sensitized, polymer, quantum dots sensitized and perovskite solar cell-type photocapacitors are developed in succession [4–7]. Among the four types of photocapacitors, toxin-free and inexpensive TiO_2 is widely used after modification or compounding with other materials as a photoelectrode [8, 9]. However, the photoelectrode requires not only complex designed components to achieve solar energy conversion, but also technological demanding of high-precision instrument for production [10, 11]. The challenge remains on the design of the phase composition with micro-/nanostructure for conveniently synthesized photoelectrode.

In a photocapacitor, TiO_2-based photoelectrode plays a major role in the absorption of photons and converts photons into electron–hole pairs [12]. TiO_2 as a semiconductor can absorb photons instantaneously which is within a UV wavelength range and owing to higher energy than the band gap energy of TiO_2 (~ 3.2 eV). High energy photons trigger electronic excitations and transitions, ultimately lead to electron–hole pairs separation

Electronic supplementary material The online version of this article (https://doi.org/10.1007/s42452-020-2884-z) contains supplementary material, which is available to authorized users.

✉ Hongfeng Yin, yinhongfeng@xauat.edu.cn; ✉ Yun Tang, tangyun@xauat.edu.cn | [1]Functional Materials Laboratory, College of Materials Science and Engineering, Xi'an University of Architecture and Technology, Xi'an 710055, China.

and result in a current flow. However, the major drawback associated with the practical application of TiO_2 is its limited band gap which can only absorb UV light that only accounts for ~ 5% of the solar spectrum [13]. In addition, the recombination of electrons and holes is related to the random transfer of activated electrons in TiO_2 which lowers the photoelectric conversion efficiency. Hence, it is necessary to control over the components and nanostructure of the TiO_2-based photoelectrode, which can overcome its inherent issues of ~ 5% low light absorption in the entire solar spectrum and reduce carrier recombination [14].

To address this issue, doping metal has been utilized to modify TiO_2. For instance, Fe has been reported as a suitable dopant to generate impurity levels in Fe–TiO_2, which can narrow the band gap to a lower level to enhance the visible light absorption [15]. The Al dopant can affect both the number and type of compensating defects in TiO_2 and make the trap of photoinjected electrons easily [16]. Coupling lower conduction band semiconductor of WO_3 (− 5.24 eV), the photogenerated electrons will transport from TiO_2 (− 4.21 eV) to WO_3 accompanied by the recombination reduction of carriers and enhancement of photocurrent under the principle of thermodynamics [17]. Constructing TiO_2 nanotube arrays in an integrated power pack can provide an efficient transport pathway for the photogenerated electrons to the current collector and lead to a total energy conversion and storage efficiency of 0.82% [18]. Therefore, the strategy of metal doping with synchronous structural designing of TiO_2 is of great research significance.

Currently, anodized Ti_3SiC_2 (ATSC) has aroused extensive attention as an energy storage material owing to the following reasons. Firstly, the substrate of layered Ti_3SiC_2 is a promising ceramic owing to good machinability (bending strength of 720 MPa), electrical (4.5 MS m^{-1}) and thermal (37 W m^{-1} K^{-1}) conductivity, which can generate the TiO_2-based composite directly via anodizing [19, 20]. The second is that the unique phase composition of TiO_2, SiO_2 and C in ATSC as effective nanoparticles can improve the specific capacitance and energy density [21]. Thirdly, the anodization is a relatively convenient approach for the fabrication of nano-array structures with large specific surface area for enormous electronic storage than conventional techniques, which commonly involve tedious processes of synthesizing and assembling [22]. In addition, the TiO_2 in ATSC can be decorated with various metal elements to enhance the limited visible light absorption of TiO_2. [23].

By taking advantage of the energy storage function of ATSC-containing photosensitive TiO_2, we demonstrate a conceptual method for the optimization of TiO_2-based photoelectrode to achieve the dual functionality of solar energy conversion and storage by introducing doping elements as shown in Scheme 1. Prior to the first process of sintering, powdered X-Si containing doping element of X is evenly mixed by wet milling with other raw materials of Ti and TiC. Then, blended powders are used for the synthesis of electric

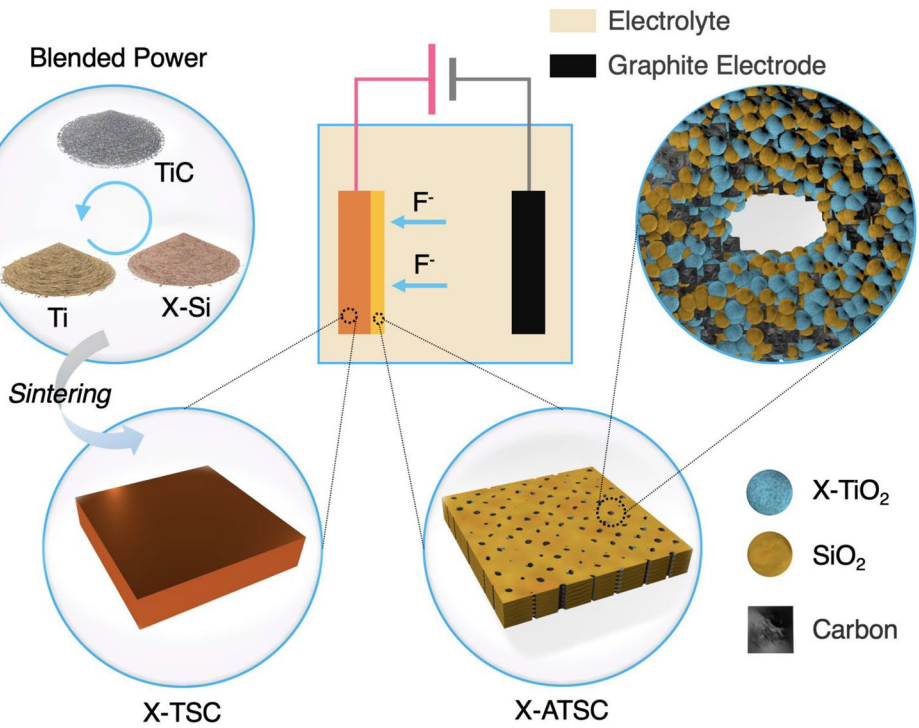

Scheme 1 Synthesis process of X-ATSC photoelectrode with introducing doping element of X

conductive ceramics of X-doped Ti_3SiC_2 (X-TSC) via a hot-pressing sintering method. Secondly, the surface of X-TSC substrate transforms into anodized phase with the assistance of an external electric field under fluorine-containing electrolyte. The specific synthesis process is shown in the Experiment Section. The above two-step synthesis is conducted to construct the anodized phase of X-TiO_2, SiO_2 and C composite with vertically ordered nanopores structure on the conductive X-TSC substrate, which make up a complete anodized X-doped Ti_3SiC_2 (X-ATSC) photoelectrode. The X-ATSC photoelectrode has three major advantages of (1) simultaneously solar energy conversion and storage abilities of the anodized phase, which have high specific surface area and abundant active energy storage sites, (2) owing self-contained current collector of X-TSC and do not require additional tedious experimental to integrate conductive substrates compared to the conventional chemical method and (3) the ordered vertical nanopores can be regarded as the bridges for the transmission of electrons between current collector and photo-conversion material. Additionally, the X of the X-TiO_2 in the anodized phase can be an advantageous doping element to further enhance the photoelectrochemical performance of X-ATSC. All advantages make it achievable to conveniently fabricate the dual-functional X-ATSC photoelectrode.

2 Experiment section

2.1 Chemicals

The raw materials for sintering are commercial powdery Ti (99.5%; 45 μm; Baoji Saite Titanium Industry Co., Ltd.), TiC (99.9%; 2.6 μm; Beijing Xingrongyuan Technology Co., Ltd.), three grades of AlSi ($Al_{0.1}Si_{0.9}$, $Al_{0.3}Si_{0.7}$ and $Al_{0.5}Si_{0.5}$; 97%; 45 μm; Nangong Ruiteng Alloy Material Co., Ltd.) and two of FeSi ($Fe_{0.25}Si_{0.75}$ and $Fe_{0.55}Si_{0.45}$; 97%; 45 μm; Nangong Ruiteng Alloy Material Co., Ltd.). Analytical grade ethylene glycol (EG) and ammonium fluoride are purchased from Sinopharm Chemical Reagent Co., Ltd., and used for anodization. All reagents are used as received without further purification.

2.2 Synthesis

Synthetic raw materials achieve a various stoichiometry of TiC:Ti:AlSi:FeSi = 2:1:0.6:0.6. The hot press sintering method is used to fabricate the pentabasic ceramic (Al, Fe–TSC) with mixed raw materials at 1500 °C for 2 h. There are six Al, Fe–TSCs in this work marked as 1-a, 1-b, 3-a, 3-b, 5-a and 5-b in sequence according to varying grades of AlSi of $Al_{0.1}Si_{0.9}$ (1), $Al_{0.3}Si_{0.7}$ (3), $Al_{0.5}Si_{0.5}$ (5) and FeSi of $Fe_{0.25}Si_{0.75}$ (a), $Fe_{0.55}Si_{0.45}$ (b). The anodization of Al, Fe–TSCs is carried out under 15 °C at 30 V for 12 h in EG electrolyte with 5 vol% water, 3 wt% NH_4F and then annealed at 500 °C for 2 h in the air for the synthesis of Al, Fe–ATSCs [21]. As shown in Table 1, correspondingly, six Al, Fe–ATSCs are marked as A1-a, A1-b, A3-a, A3-b, A5-a and A5-b.

2.3 Characterization

For the three-point bending strength test, Al, Fe–TSCs are cut into rectangular bars of 4 mm × 3 mm × 40 mm and tested using a Universal Testing Machine (WDW-300) with loading speed of 0.5 mm min^{-1}. The digital conductivity meter (Sigma 2008 A1) is used to test the electrical conductivity. Phase composition of the Al, Fe–TSCs is identified by powder X-ray diffraction (XRD, DMAX-2400) with Cu-Kα X-ray radiation ($\lambda = 0.154$ nm). The microstructure of Al, Fe–TSCs and Al, Fe–ATSCs is examined by field emission scanning electron microscope (FE-SEM, SU-8010). The surface chemical composition of Al, Fe–ATSCs is analyzed by X-ray photoelectron spectroscopy (XPS, Krato Axis Ultra DLD), and the XPS spectra are calibrated, refer to the C 1*s* peak at 284.6 eV. UV–Vis diffuse reflectance spectra (DRS) of Al, Fe–ATSCs are acquired on the spectrometer (PE Lambda 950) at room temperature.

2.4 Photoelectrochemical (PEC) measurements and calculation

The PEC performance of Al, Fe–ATSCs cut into 5 × 10 × 10 mm disks is evaluated using the CHI660E workstation with a three-electrode setup in 1 mol L^{-1} Na_2SO_4 aqueous electrolyte at room temperature. Al, Fe–ATSCs are directly used as the working electrode with an active area of 1 cm^2. The Ag/AgCl electrode and platinum foil are used as the reference electrode and the counter electrode.

Table 1 Compositions and IDs of the samples

Composition	$Ti_3Al_{0.06}Fe_{0.15}Si_{0.99}C_2$	$Ti_3Al_{0.06}Fe_{0.33}Si_{0.81}C_2$	$Ti_3Al_{0.18}Fe_{0.15}Si_{0.87}C_2$	$Ti_3Al_{0.18}Fe_{0.33}Si_{0.69}C_2$	$Ti_3Al_{0.3}Fe_{0.15}Si_{0.75}C_2$	$Ti_3Al_{0.3}Fe_{0.33}Si_{0.57}C_2$
Sample IDs	1-a	1-b	3-a	3-b	5-a	5-b
(After anodization)	A1-a	A1-b	A3-a	A3-b	A5-a	A5-b

The potential window for all PEC measurements is from −0.5 to 0.5 V. The cyclic voltammetry (CV) measurement is conducted at varied scan rates from 10 to 100 mV s^{-1}. The galvanostatic charge/discharge (GCD) measurement is applied to characterize the specific capacitance which is calculated as the equation of $C = I \cdot \Delta t / A \cdot V$, where I is the discharge current, Δt is the discharge time, A is the area of electrode, and V is voltage range of each scan. Electrochemical impedance spectroscopy (EIS) results are obtained at the amplitude of 5 mV in the frequency range from 100 kHz to 0.01 Hz. To investigate the photoresponse characteristics, Al, Fe–ATSCs are illuminated under 80 mW cm^{-2} under a 500 W xeon lamp with a 420-nm cutoff filter.

3 Results and discussion

Herein, this study involves three grades of AlSi including $Al_{0.1}Si_{0.9}$, $Al_{0.3}Si_{0.7}$, $Al_{0.5}Si_{0.5}$ and two FeSi of $Fe_{0.25}Si_{0.75}$ and $Fe_{0.55}Si_{0.45}$ to achieve different levels of Al and Fe doping. After first process of sintering, six doped Ti_3SiC_2 samples with two elements of Al and Fe simultaneously (Al, Fe–TSCs) are labeled as 1-a, 1-b, 3-a, 3-b, 5-a, 5-b, which refer to raw materials of $Al_{0.1}Si_{0.9}$ (1), $Al_{0.3}Si_{0.7}$ (3), $Al_{0.5}Si_{0.5}$ (5), $Fe_{0.25}Si_{0.75}$ (a), $Fe_{0.45}Si_{0.55}$ (b). Variation in mechanical and physical properties can reflect different phase compositions of samples. The bending strength at room temperature of Al, Fe–TSCs is illustrated in Figure S1. When the molar amount of doped Al is constant, the bending strength decreases with the increase in molar amount of Fe. However, dissimilar to the trends observed in changing the doping amount of Fe, when the $Fe_{0.25}Si_{0.75}$ is a dopant, the bending strength of Al, Fe–TSCs kept increasing from 333.08 MPa of 1-a to 353.53 MPa of 3-a with the increase in molar amount of doping Al. Moreover, the highest bending strength of 444.38 MPa for 5-a and the lowest of 234.78 MPa for 1-b among Al, Fe–TSCs are observed. All of these data highlighted that the suitable doping amount of Al and Fe is significantly reinforcement for the bending strength among Al, Fe–TSCs. Figure 1a shows the electric conductivity of Al, Fe–TSCs, similar to the trends of bending strength; the $Fe_{0.25}Si_{0.75}$ is with increasing molar amount of Al from $Al_{0.1}Si_{0.9}$ to $Al_{0.3}Si_{0.7}$ synthesized Al, Fe–TSCs show higher conductivity of 0.87 MS m^{-1} to 1.04 MS m^{-1} compared to the $Fe_{0.45}Si_{0.55}$ synthesized samples. It is also the 5-a reaching the maximum electric conductivity of 2.18 MS m^{-1} and the relatively lower conductivity of 0.65 MS m^{-1} for 1-b among Al, Fe–TSCs. Statistically significant change in both bending strength and electric conductivity is corresponding to the phase composition in Al, Fe–TSCs.

To understand the effects of Al and Fe dopants on the crystal structure and inherent physical properties of Al, Fe–TSCs, X-ray diffractions (XRD) are carried out as

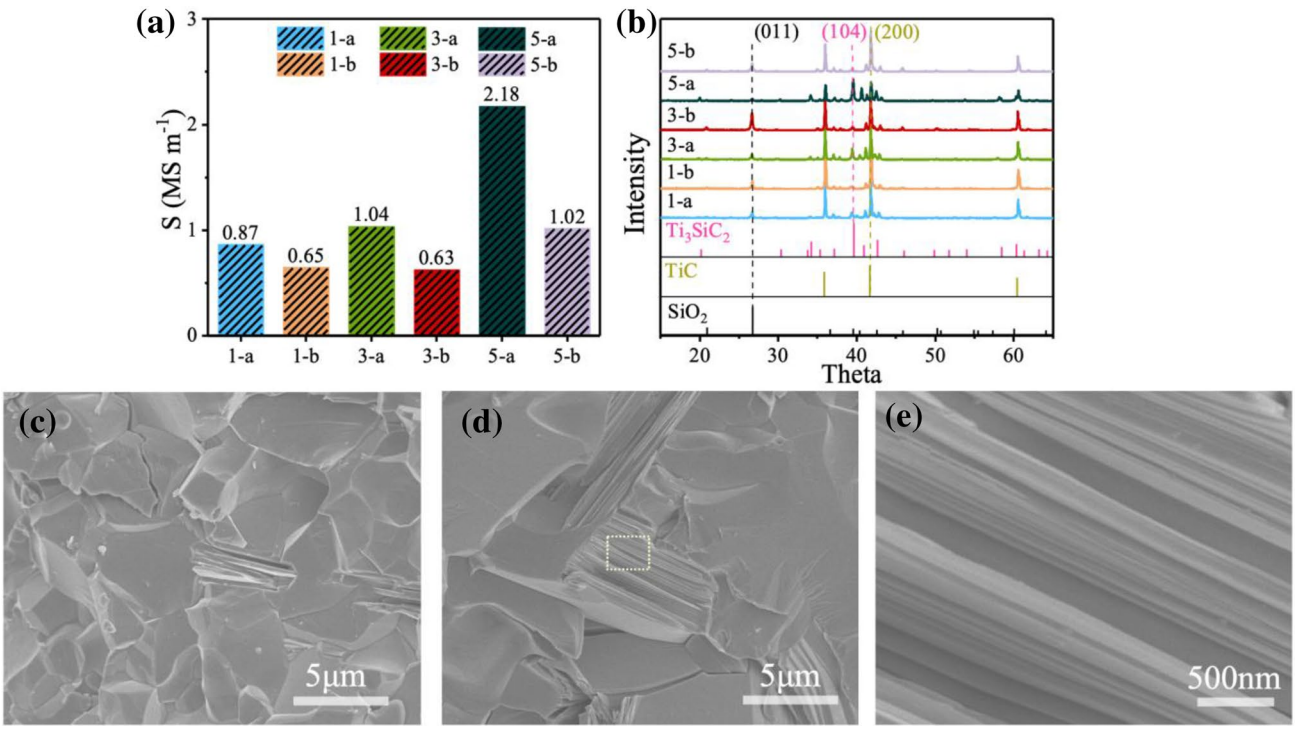

Fig. 1 **a** Electric conductivity and **b** XRD patterns of the synthesized Al, Fe–TSCs. SEM images of the **c** 1-b and **d** 5-a with **e** partial enlargement

depicted in Fig. 1b. With the systematic amount of Al and Fe dopants, the peaks in all Al, Fe–TSCs are assigned to the main phase of Ti_3SiC_2 (JCPDS No. 74-0310) or TiC (JCPDS 32-1393). The main phase of TiC can be identified with few detected SiO_2 and Ti_3SiC_2 in Al, Fe–TSCs synthesized with $Fe_{0.45}Si_{0.55}$. Therefore, solid solution content of Fe in Ti_3SiC_2 should have a limit value. However, the (104) main peaks of Ti_3SiC_2 in the $Fe_{0.25}Si_{0.75}$ synthesized Al, Fe–TSCs are shifted to the higher angle values with increment of Al content from $Al_{0.1}Si_{0.9}$ to $Al_{0.5}Si_{0.7}$, which reveal the slight decrease in lattice parameter of Ti_3SiC_2 due to the incorporation of Al into the Ti_3SiC_2 host lattice. Accordingly, there is available Al atoms diffusion into the Ti_3SiC_2 phase. The above results demonstrate that the formation of doped Ti_3SiC_2 phase requires a relatively small amount of doping Fe, such as 1-a, 3-a and 5-a. Otherwise, TiC will be the main phase, like 1-b, 3-b and 5-b. Further, the co-doping of Al and Fe in 5-a is proved by Figure S2. From the atomic ratio of Al and Al + Si + Fe as shown in Figure S3, it can be inferred that the successful doping amount of Al in Ti_3SiC_2 is 15.9% and Fe is 0.1%. The observation indicates that the presence of doped Ti_3SiC_2 is the reason why 5-a has both higher bending strength and electric conductivity than 1-b, which refer to the Ti_3SiC_2 owing to better mechanical properties and electrical conductivity than TiC [19]. Furthermore, Si exists in the form of SiO_2 or doped Ti_3SiC_2. In 1-b, 3-b and 5-b when the SiO_2 content is higher and the doped Ti_3SiC_2 content is lower, the conductivity and bending strength are lower than 1-a, 3-a and 5-a, which corresponds to the relatively good mechanical properties and electrical conductivity of Ti_3SiC_2. Correspondingly, Fig. 1c, d illustrates the surfaces of the 1-b and 5-a, and the 5-a possesses flatter surface with multilayered structure than 1-b, consistent with XRD analysis results that 5-a has a homogeneous distribution of Al- and Fe-doped Ti_3SiC_2. Figure 1e is an enlargement of the rectangular mark in Fig. 1d which clearly confirms the nanolayered characteristic of doped Ti_3SiC_2 phase with the dimensions of ~ 10 nm in the 5-a.

After the second process of anodizing, Al, Fe–TSCs of 1-a, 1-b, 3-a, 3-b, 5-a and 5-b are transformed into Al, Fe–ATSCs of A1-a, A1-b, A3-a, A3-b, A5-a and A5-b. XPS spectra of Al, Fe–ATSCs are shown in Fig. 2 to elucidate the surface chemical composition of the oxide composites surfaces. All of the full-scale spectra in Fig. 2a demonstrate the presence of Ti, Si, C and O with small amount of Al and Fe. Further, the different surface bonding configurations of elements on A5-a and A1-b have been obtained from the

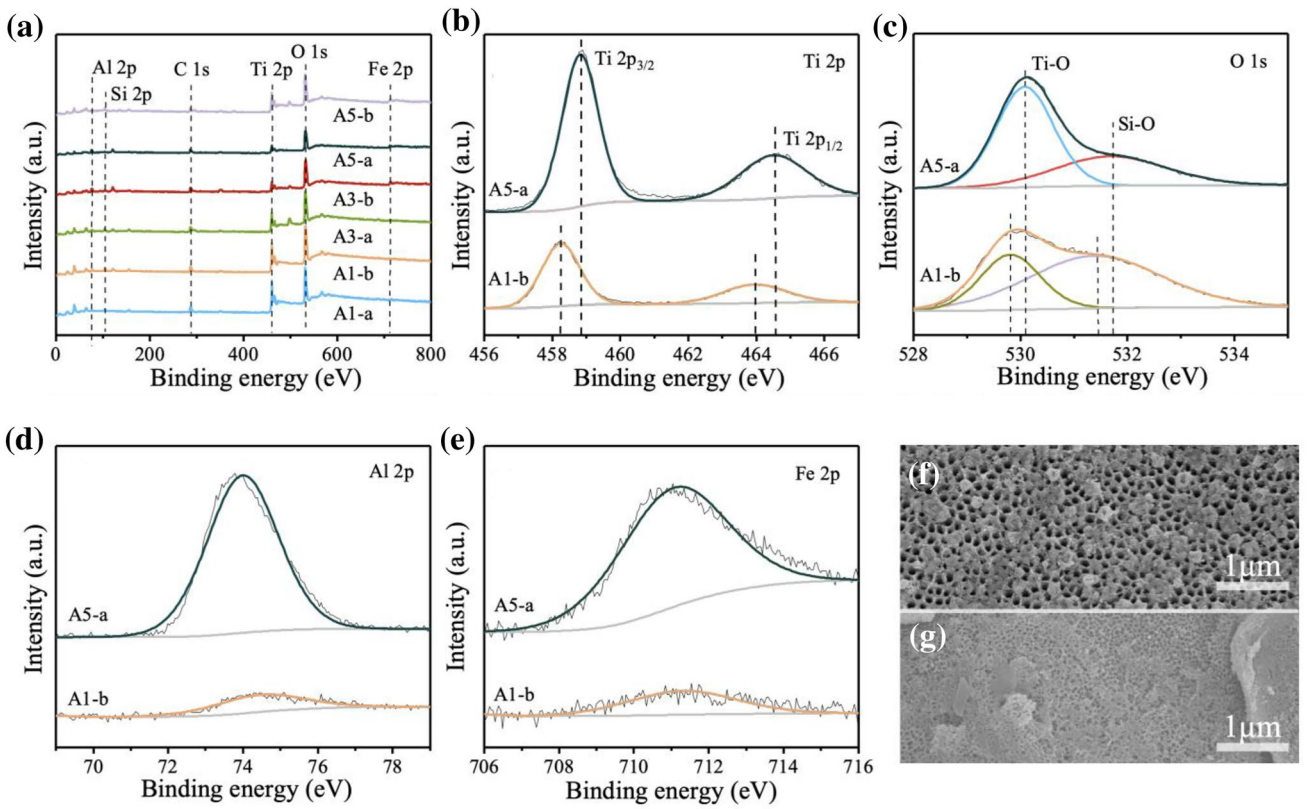

Fig. 2 XPS spectra of **a** the survey for Al, Fe–ATSCs, **b** Ti 2*p*, **c** O 1*s*, **d** Al 2*p* and **e** Fe 2*p* for the A5-a and A1-b. SEM images of **f** A5-a and **g** A1-b

deconvoluted XPS spectra of four interesting regions (Ti, O, Al, and Fe). As shown in Fig. 2b, owing to the spin–orbit splitting, there are two peaks in Ti 2*p* spectra of A1-b assigned to TiO_2 (458.2 and 463.9 eV). However, peaks in A5-a are shifted to the higher binding energy (458.9 and 464.6 eV) than A1-b indicating that both Al and Fe have existed in the lattice of TiO_2 and formed Al and Fe co-doped TiO_2 (Al, Fe–TiO_2). The O 1*s* spectra of A1-b in Fig. 2c can be deconvoluted into two peaks at 529.8 and 531.5 eV corresponding to TiO_2 and SiO_2, respectively. Consistent with Ti 2*p*, the binding energy of O 1*s* for TiO_2 in A5-a (430.1 eV) is higher than A1-b which confirms the formation of Al, Fe–TiO_2. Compared with A5-a, it is obvious that the SiO_2 content in A1-b is relatively higher than TiO_2. From the previous XRD analysis, the Si element in 1-b is present in the form of SiO_2, and in 5-a is Ti_3SiC_2. Consequently, under the joint action of the electric field and acidic etching conditions, the Si element in Ti_3SiC_2 is more easily selectively etched than the SiO_2. In addition, referring to Fig. 2c with the similar intensity of O 1*s* in both A5-a and A1-b, the presence of Al and Fe element of A1-b in Fig. 2d, e exhibits relatively inconspicuous peaks than A5-a. XPS results indicate that the Ti, Si, Al and Fe elements are selectively etched accompanied with residual carbon. Then, a small amount of Si is oxidized to SiO_2. Ti is further oxidized with the generation of Al, Fe–TiO_2 in A5-a, which is strongly demonstrated by the binding energy peaks offset in Ti 2*p* and O 1*s* relative to A1-b. Moreover, after anodization, the main phase of TiC in 1-b is transformed into TiO_2 in A1-b, and the Al, Fe–Ti_3SiC_2 in 5-a into Al, Fe–TiO_2 which is also demonstrated in Figure S4 and Figure S5. The SEM image of A5-a is shown in Fig. 2f; the periodical compactly arranged nanopores with diameter of ~ 100 nm are clearly observed. However, from the morphology of A1-b in Fig. 2g, the nanoporous surface with significantly smaller diameter under 40 nm is not as uniform as A5-a. Furthermore, nanopores connect to the neighboring nanopores through the necks, suggesting the good electronic transmission and storage capacity of A5-a.

Cyclic voltammetry (CV) curves in Fig. 3a clearly show that Al, Fe–ATSCs can function as electrode materials for redox capacitors. Both of the CVs and galvanostatic charge–discharge (GCD) curves (Fig. 3b) between − 0.5 and 0.5 V show typical capacitive characteristics. According to the symmetric GCDs, the areal specific capacitance of the photoelectrodes is calculated to be 11.04, 7.56, 4.98, 11.31, 12.03 and 11.31 mF cm^{-2} for A1-a, A1-b, A3-a, A3-b, A5-a and A5-b at 100 mV s^{-1}, respectively [24]. The Si element in both of the SiO_2 and Ti_3SiC_2 is partially selectively etched by fluoride ions and dissolved in the electrolyte, thus leaving the anodized doped Ti_3SiC_2 layer with nanoporous array. The higher capacitance performance of A1-a, A3-a and A5-a indicates that the more Si elements are selectively etched from doped Ti_3SiC_2 than A1-b, A3-b and A5-b, respectively, while A3-b shows the lowest capacitance corresponding to the highest SiO_2 phase as shown in Fig. 1b which results in the lowest anodized doped Ti_3SiC_2 after anodizing. The relatively highest specific capacitance among these electrodes is delivered by A5-a of 12.03 mF cm^{-2} which is attributed to periodical arranged nanopores on the uniform surface for the large amount of charge storage sites. As shown in Fig. 3c, observed similarly shaped CV curves of A5-a at different scan rates from 10 to 100 mV s^{-1} represent the good reversibility of capacitive behavior. Meanwhile, a couple of obvious redox peaks at ~ 0.2 V and 0 V under 10 mV/s in Fig. 3c are correlated with the reversible reaction of O^{2-}/O_2 for the sodiation/desodiation processes in the Na_2SO_4 electrolyte, suggesting that pseudocapacitance contributions of charging and discharging are happening near the electrolyte–electrode interfaces [25]. Figure 3d shows the cycle ability of A5-a, the capacitance still with high retention of 93% compared to its initial value after 1000 charge/discharge cycles, representing an excellent cycling stability of Al, Fe–ATSC capacitor.

Electrochemical impedance spectroscopy (EIS) is a powerful tool to assess the electron transfer behavior and equivalent series resistance of a capacitor [26]. Figure 4 depicts the Nyquist plot in the frequency range from 0.01 Hz to 100 kHz before and after cycling stability test. Generally speaking, at high frequency, the intercept of the impedance spectrum on the *X* axis is ascribed to the series resistance (R_s) between the active material (anodized surface) and current collector (Al, Fe–TSC substrate) [27]. The diameter of the semicircle is related to the electron transfer resistance (R_{ct}) at the electrode surface, and the smaller diameter indicates the lower R_{ct}. Clearly, the 1.07 Ω of R_s and 5.16 Ω of R_{ct} for A5-a are very small, indicating fast ion transport and low resistance in the electrode. At low frequency, the Warburg resistance is reflected by a straight line with a phase angle of about 45° for the influence of the electrode porosity [28]. The larger the slope of the low frequency line, the closer to the ideal supercapacitor. It is observed that the low-frequency line deviates little after the cycling test, demonstrating the good stability with a capacity loss of about 7% to its initial. Overall, the remarkable specific capacitance of A5-a could be ascribed to the unique phase composition, the uniform morphology and the obvious pseudocapacitance.

Photocurrents of Al, Fe–ATSCs under visible light irradiation of 80 mW cm^{-2} in Fig. 5a are used to evaluate the absorption of photons and separation of electron/hole pairs. Among the contrasting photocurrents, the A5-a shows the highest photocurrent density of 59 μA cm^{-2} at 0 V lasted for 500 s than that of the other photoelectrodes. The excellent photo-switching property of A5-a is affirmed by fast photocurrent response, whose value rises up to 30

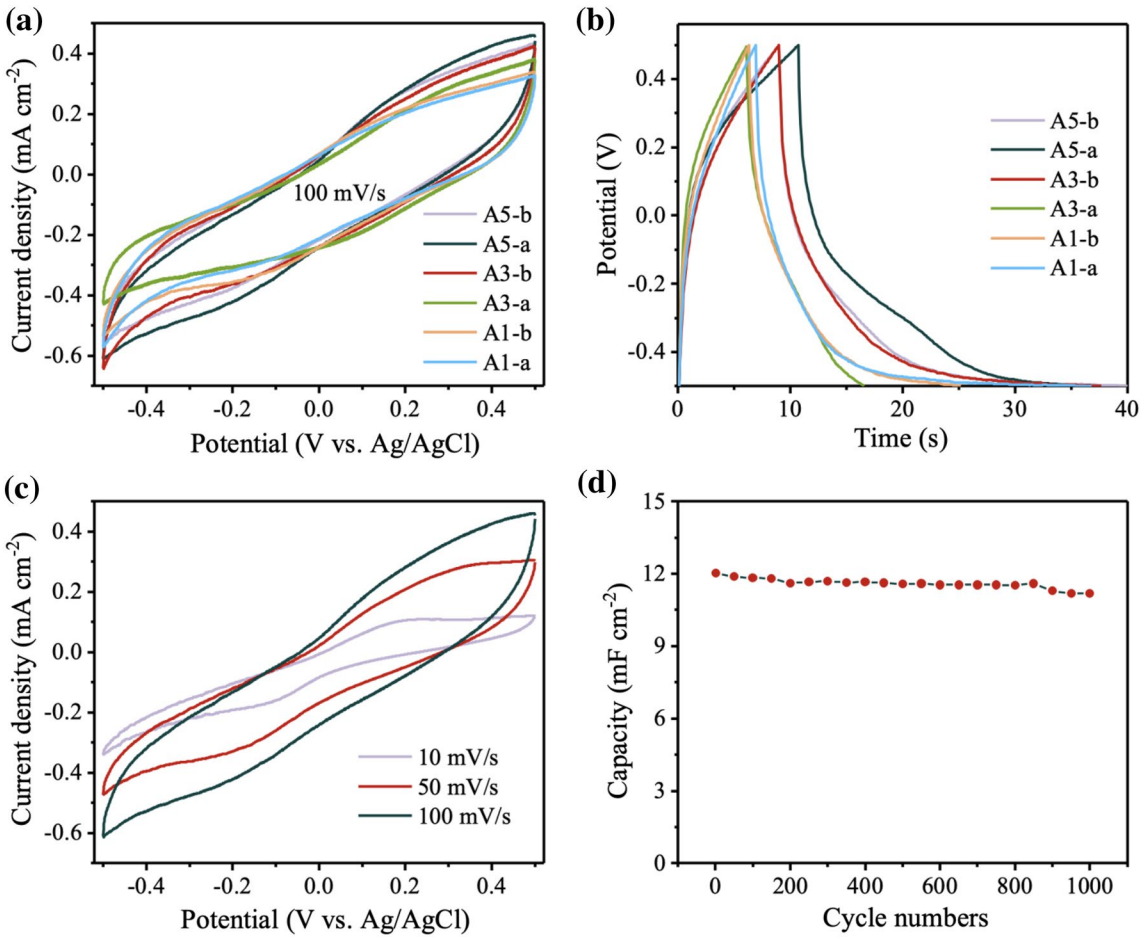

Fig. 3 **a** CVs at 100 mV s^{-1} and **b** GCDs at 0.3 mA cm^{-2} of Al, Fe–ATSCs from −0.5 to 0.5 V. **c** CVs with different scanning rates and **d** cycle stability of A5-a

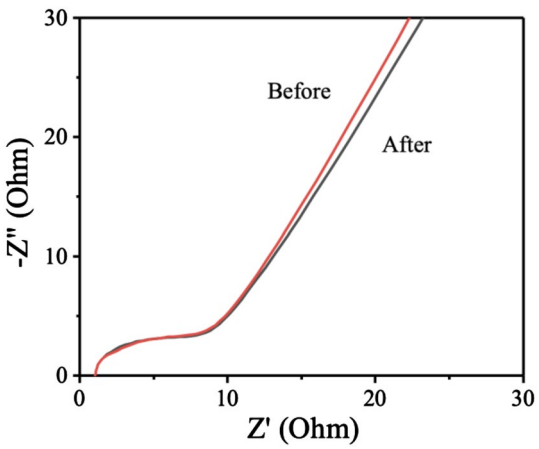

Fig. 4 **a** Nyquist plots in the frequency range from 0.01 Hz to 100 kHz of A5-a before and after the cycling test

μA cm^{-2} immediately at the moment of turning on the light and rapidly reduces from 52 to 0 μA cm^{-2} at turning off. The fast photocurrent response in A5-a implies that under visible light condition, photons rapidly transform into excitons, and excitons quickly separate into electron–hole pairs which are attributed to the periodic nanopores structure with large specific surface area for light harvesting and ordered channels for charge transportation. In addition, the continuous increase in photocurrent from 40 to 59 μA cm^{-2} is on account of the synergy of introducing the Al and Fe into TiO_2 of A5-a. The photocharging and galvanostatic discharging processes of Al, Fe–ATSCs for the potential versus time characteristics are shown in Fig. 5b. Consistent with the photocurrent test, A5-a exhibits the highest storage capacity than the others. When the light is turned on to trigger the photocharge process under visible light illumination, the photoelectrons generated in the doped TiO_2 of A5-a are separated and collected by the photoelectrode which can be charged to 0.04 V in 13 s. After that, all of the photoelectrodes are discharged at a

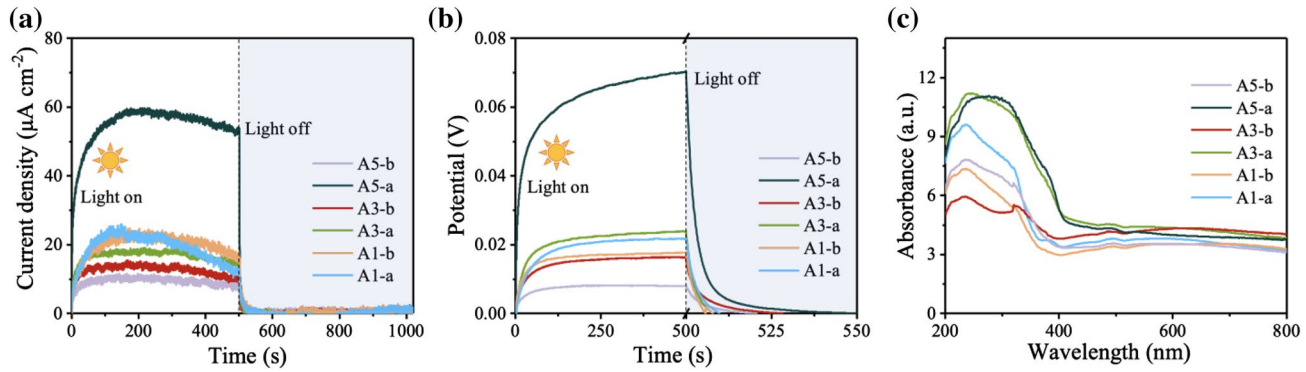

Fig. 5 **a** Photocurrents response and **b** photo-charge/discharge in the presence of visible light illumination and in dark condition, and **c** UV–Vis diffuse reflectance spectra of Al, Fe–ATSCs

current density of 3 μA cm^{-2} in dark expect for the A5-a at 6 μA cm^{-2}, whereas the discharge time of 50.5 s for A5-a is obviously longer than others which still refers to the highest calculated capacitance of 4.33 mF cm^{-2}. Further, the specific capacitance of A5-a is 3.2 times higher than A1-b of 1.33 mF cm^{-2}. The large promotion of capacitance could originate from the increased redox reaction sites by high molar ratio Al doping of A5-a with high defect concentration than other photoelectrodes [29]. A5-a owing to the best photoresponse performance is also related to its highest conductivity of the substrate among all samples, which can transfer the photogenerated electrons quickly. Besides, the highest conductivity is related to the highest doped Ti_3SiC_2 phase content, and thus, it can produce more photoresponsive TiO_2-based composite after anodizing with higher photoelectric conversion efficiency.

As shown in Fig. 5c, UV–Vis diffuse reflectance spectroscopy (DRS) is employed to explore the light absorption capability of Al, Fe–ATSCs which exhibit both absorption of ultraviolet light and visible light. It is clear that the DRS spectra of the A5-a and A3-a demonstrate the significant absorption edge at 455.40 nm and 470.59 nm in the visible region with enhanced absorption intensity than other samples. Appropriate amount of Al- and Fe-doped TiO_2 can improve their visible light absorption for high charge separation efficiency, which is mainly ascribed to the Al and Fe atoms occupying the interstitial sites in the TiO_2 lattice and lead to an increase in defect concentration and an impurity doping level. Consistent with the discussion of XRD, XPS and DRS, the suitable amount of dopant in Al, Fe–ATSCs can enhance the charge storage and light harvesting not only in the ultraviolet region but also in the visible portion. The current–voltage (*J*–*V*) response is graphically illustrated in Figure S7. The photocapacitor investigated in this study shows a solar power conversion efficiency (PCE) of 0.015%, which is as low as the previous study (0.02%) [30]. This low value of the PCE is mainly attributed to the low transparency of the oxide layer with limited flow of the photons–electrons conversion during the charging process. However, this study for the first time explores the feasibility for anodized doped Ti_3SiC_2 as a photocapacitor which do not require additional assembly processes as traditional integrated photocapacitors.

The strategy for photoelectrode design of doping TiO_2 composite with two elements simultaneously via anodizing is feasible. Composition in Al, Fe–ATSC plays an important role in gaining insights into the enhanced performance mechanism with the modulation of Al and Fe. The low capacitance and solar conversion performance for the high doping content of Fe in Al, Fe–ATSC can be explained by the excessive Fe suppressing the generation of conductive Al, Fe–Ti_3SiC_2, which further be anodized into Al, Fe–TiO_2 composite with periodic nanopores structure. However, at the relatively small amount of Fe doping, the photoelectrode fabricated with high molar doping content of Al in Al, Fe–ATSC exhibits better performance than the rest. The high concentration of Al dopant in Al, Fe–ATSC will generate defects in the main phase of Al, Fe–TiO_2 and facilitate the pseudocapacitive energy storage. In addition, the semiconductor of Al, Fe–TiO_2 in Al, Fe–ATSC can absorb photons and generate electron–hole pairs under visible light illumination. The photogenerated electrons can easily move to the conduction band of Al, Fe–TiO_2, and then, excited electrons are facilely transported and collected by the conductive nanopores skeleton composed of Al, Fe–TiO_2, SiO_2 and C on the Al, Fe–TSC substrate. Meanwhile, significantly enhanced performance of capacitance, solar conversion and storage of the photoelectrode can be promoted to 12.03 mF cm^{-2}, 59 μA cm^{-2} and 4.33 mF cm^{-2}.

4 Conclusions

In summary, an individual integrated Al, Fe–ATSC photoelectrode including substrate and anodized surface with the dual function of solar conversion and capacitive energy storage has been designed and developed by two-step method of sintering and anodizing. Al- and Fe-doped Ti_3SiC_2 substrate is sintered at the low and high content of doping Fe and Al (with raw material $Fe_{0.25}Si_{0.45}$ and $Al_{0.5}Si_{0.5}$) which possesses the higher bending strength and conductivity than others. Photogenerated electrons and holes from the main phase of Al, Fe–TiO_2 on the anodized surface of Al, Fe–ATSC are transferred and electrochemically stored in the periodic nanopores structure with large interface area to facilitate the charge separation. Such a system delivers a maximum specific capacitance up to 12.03 mF cm^{-2} at the scan rate of 100 mV s^{-1} with the superior photoresponse of 59 μA cm^{-2} and photo-capacitance of 4.33 mF cm^{-2}. The presented approach is able to pave a new avenue for the design of various heterojunction photoelectrodes with vertically aligned nanopores for both solar energy conversion and storage.

Compliance with ethical standards

Conflict of interest We confirm that there is non-financial conflict of interest for this work. The manuscript has been read and approved by all named authors, and there are no other persons who satisfied the criteria for authorship but are not listed. We confirm that we have given due consideration to the protection of intellectual property associated with this work and that there are no impediments to publication, including the timing of publication, with respect to intellectual property.

References

1. Wang W, Qi L (2019) Light Management with patterned micro- and nanostructure arrays for photocatalysis, photovoltaics, and optoelectronic and optical devices. Adv Funct Mater 29:1807275
2. Üzer E, Kumar P, Kisslinger R, Kar P, Thakur UK, Zeng S, Shankar K, Nilges T (2019) Vapor deposition of semiconducting phosphorus allotropes into TiO_2 nanotube arrays for photoelectrocatalytic water splitting. ACS Appl Nano Mater 2:3358–3367
3. Miyasaka T, Murakami TN (2004) The photocapacitor: an efficient self-charging capacitor for direct storage of solar energy. Appl Phys Lett 85:3932–3934
4. Yang Z, Li L, Luo Y, He R, Qiu L, Lin H, Peng H (2013) An integrated device for both photoelectric conversion and energy storage based on free-standing and aligned carbon nanotube film. J Mater Chem A 1:954–958
5. Wee G, Salim T, Lam YM, Mhaisalkar SG, Srinivasan M (2011) Printable photo-supercapacitor using single-walled carbon nanotubes. Energy Environ Sci 4:413–416
6. Narayanan R, Kumar PN, Deepa M, Srivastava AK (2015) Combining energy conversion and storage: a solar powered supercapacitor. Electrochim Acta 178:113–126
7. Xu J, Ku Z, Zhang Y, Chao D, Fan HJ (2016) Integrated photo-supercapacitor based on PEDOT modified printable perovskite solar cell. Adv Mater Technol 1:1600074
8. Ng CH, Lim HN, Hayase S, Harrison I, Pandikumar A, Huang NM (2015) Potential active materials for photo-supercapacitor: a review. J Power Sources 296:169–185
9. Huang J, Wang Y, Liu X, Li Y, Hu X, He B, Shu Z, Li Z, Zhao Y (2019) Synergistically enhanced charge separation in $BiFeO_3$/Sn:TiO_2 nanorod photoanode via bulk and surface dual modifications. Nano Energy 59:33–40
10. Meng H, Pang S, Cui G (2019) Photo-supercapacitors based on third-generation solar cells. Chemsuschem. https://doi.org/10.1002/cssc.201900398
11. Khamwannah J, Zhang Y, Noh SY, Kim H, Frandsen C, Kong SD, Jin S (2012) Enhancement of dye sensitized solar cell efficiency by composite TiO_2 nanoparticle/8 nm TiO_2 nanotube paper-like photoelectrode. Nano Energy 1:411–417
12. Falk M, Shleev S (2019) Hybrid dual-functioning electrodes for combined ambient energy harvesting and charge storage: towards self-powered systems. Biosens Bioelectron 126:275–291
13. Wang Y, Zhang F, Yang M, Wang Z, Ren Y, Cui J, Zhao Y, Du J, Li K, Wang W, Kang DJ (2019) Synthesis of porous MoS_2/CdSe/TiO_2 photoanodes for photoelectrochemical water splitting. Microporous Mesoporous Mater 284:403–409
14. Zhao XG, Huang LQ (2017) Iridium, carbon and nitrogen multiple-doped TiO_2 nanoparticles with enhanced photocatalytic activity. Ceram Int 43:3975–3980
15. Wang Z, Yin H, Tang Y, Siyal SH, Yuan H (2019) Electrochemical and photo response behavior of in situ Fe doped Ti_3SiC_2 after anodization. Int J Hydrogen Energy. https://doi.org/10.1016/j.ijhydene.2019.03.199
16. Murashkina AA, Murzin PD, Rudakova AV, Ryabchuk VK, Emeline AV, Bahnemann DW (2015) Influence of the dopant concentration on the photocatalytic activity: Al-doped TiO_2. J Phys Chem C 119:24695–24703
17. Liu Y, Xie C, Li J, Zou T, Zeng D (2012) New insights into the relationship between photocatalytic activity and photocurrent of TiO_2/WO_3 nanocomposite. Appl Catal A 433:81–87
18. Guo W, Xue X, Wang S, Lin C, Wang Z (2012) An integrated power pack of dye-sensitized solar cell and Li battery based on double-sided TiO_2 nanotube arrays. Nano Lett 12:2520–2523
19. Sun ZM (2013) Progress in research and development on MAX phases: a family of layered ternary compounds. Int Mater Rev 3:143–166
20. Tesfaye A, Mashtalir O, Naguib M, Barsoum MW, Gogotsi Y, Djenizian T (2016) Anodized Ti_3SiC_2 as an anode material for Li-ion microbatteries. ACS Appl Mater Interface 8:16670–16676
21. Wang Z, Yin H, Tang Y, Hou Q, He C, Yuan H (2019) Reinforced photoelectrochemical properties of nanostructural TiO_2/C/SiO_2 integrated on conductive Ti_3SiC_2. Ceram Int 45:7253–7261
22. Mohamed AER, Rohani S (2011) Modified TiO_2 nanotube arrays (TNTAs): progressive strategies towards visible light responsive photoanode, a review. Energy Environ Sci 4:1065–1086
23. Yin H, Wang Z, Tang Y, Chourashiya M, Li X, Yuan H, Yan N, Ren X (2020) Different enhancement mechanisms of the anodizing Al-doped or Sn-coupled Ti_3SiC_2 for the photoelectrochemical performance. ChemistrySelect 5:1496–1505
24. Alinajafi HA, Ensafi AA, Rezaei B (2018) Reduced graphene oxide decorated with thionine, excellent nanocomposite material for a powerful electrochemical supercapacitor. Int J Hydrogen Energy 43:19102–19110
25. Li W, Fukunishi M, Morgan BJ, Borkiewicz OJ, Chapman KW, Pralong V, Maignan A, Lebedev OI, Ma J, Groult H, Komaba S,

Dambournet D (2017) A reversible phase transition for sodium insertion in anatase TiO_2. Chem Mater 29:1836–1844
26. Xing LB, Hou SF, Zhou J, Li S, Zhu T, Li Z, Si W, Zhuo S (2014) UV-assisted photoreduction of graphene oxide into hydrogels: high-rate capacitive performance in supercapacitor. J Phys Chem C 118:25924–25930
27. Li L, Zhang X, Wu G, Peng X, Huo K, Chu PK (2015) Supercapacitor electrodes based on hierarchical mesoporous MnO_x/nitrided TiO_2 nanorod arrays on carbon fiber paper. Adv Mater Interfaces 2:1400446
28. Wang L, Gao Z, Chang J, Liu X, Wu D, Xu F, Guo Y, Jiang K (2015) Nitrogen-doped porous carbons as electrode materials for high-performance supercapacitor and dye-sensitized solar cell. ACS Appl Mater Interfaces 7:20234–20244
29. Murashkina AA, Rudakova AV, Ryabchuk VK, Nikitin KV, Mikhailov RV, Emeline AV, Bahnemann DW (2018) Influence of the dopant concentration on the photoelectrochemical behavior of Al-doped TiO_2. J Phys Chem C 122:7975–7981
30. Bae J, Park Y, Lee M, Cha S, Choi Y, Lee C, Kim J, Wang Z (2011) Single-fiber-based hybridization of energy converters and storage units using graphene as electrodes. Adv Mater 23:3446–3449